A COMPARISON OF THEORY AND EXPERIMENT FOR COUPLED ROTOR-BODY STABILITY OF A HINGELESS ROTOR MODEL IN HOVER

William G. Bousman
Research Scientist
U.S. Army Aeroflightdynamics Directorate
Ames Research Center

Abstract

Three cases were selected for correlation from an experiment that examined the aeromechanical stability of a small-scale model of a hingeless rotor and fuselage in hover. The first case examined the stability of a configuration with 0° blade pitch so that coupling between dynamic modes was minimized. The second case was identical to the first except the blade pitch was set to 9° which provides flap-lag coupling of the rotor modes. The third case had 9° of blade pitch and also included negative pitch-lag coupling, and therefore was the most highly coupled configuration. Analytical calculations were made by Bell Helicopter Textron, Boeing Vertol, Hughes Helicopters, Sikorsky Aircraft, the U.S. Army Aeromechanics Laboratory, and NASA Ames Research Center and compared to some or all of the experimental cases. Overall, the correlation ranged from very poor-to-poor to good.

Introduction

As a part of the Methodology Assessment, three cases were selected from the experiment reported in Ref. 1 for comparison with theoretical calculations. The three cases differ only in the type and extent of aeroelastic coupling in the rotor. Case 1 represents the simplest configuration with the blade pitch angle set to 0° to minimize coupling. Structural flap-lag coupling is incorporated in Case 2 by setting the blade pitch angle to 9°. Case 3 is the most complex configuration with flap-lag coupling combined with negative pitch-lag coupling. The three cases provide a graduated series for aeromechanical stability with increasing complexity in the rotor aeroelastic coupling. Therefore, they provide a good test of the capability of theoretical models to predict stability as the aeroelastic coupling becomes more complex.

The theoretical models that were compared with the data include the Bell Helicopter Textron DRAV21 code, the Boeing Vertol C-90, the Hughes Helicopter DART and E927-1 analyses, Sikorsky Aircraft G400 code, and the U.S. Army Aeromechanics Laboratory FLAIR analysis. The Sikorsky Aircraft E927-2 and E927-3 codes, and the NASA Ames Research Center CAMRAD, were compared with some of the data.

The paper will briefly describe the experiment from which these data were obtained and then present the correlation. The agreement between theory and experiment will be discussed. The appendices document the experimental model properties, tabulate the experimental data points, and show all of the comparisons.

Experiment Description

The model rotor and fuselage used in the experiment is shown in Fig. 1. The rotor has three blades that are mounted on root flexures that allow flap and lead-lag motion. The flexures are mounted to a hub which is supported by bearings on a static mast. The static mast is bolted to a transmission with a water-cooled electric motor at either end that represents the fuselage. The rotor and fuselage are supported in a gimbal frame with flexure pivots that allow pitch and roll motions. Springs are connected across the gimbal pivots to provide frequencies that are representative of actual helicopters; the pitch and roll inertias are appropriately scaled. The stand is stiffened below the gimbal so that the stand frequencies are higher than the body frequencies by a factor of 10.

The regressing lead-lag mode was excited with a floor-mounted 50-lb shaker that oscillates the

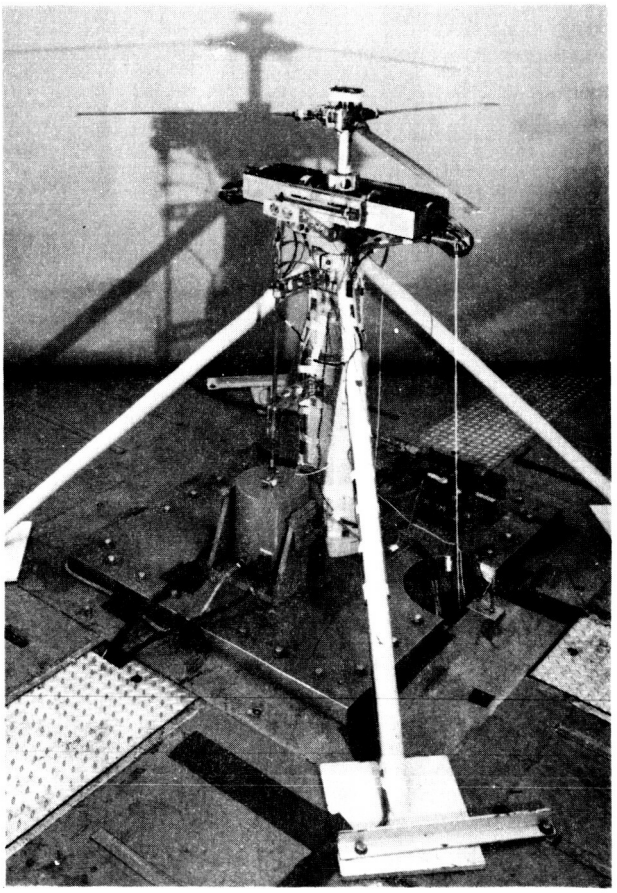

Fig. 1 Three-bladed hingeless rotor model mounted to gimbal frame and stand.

model about the roll gimbal. When a sufficient level of excitation was achieved, a pneumatic clamp was opened and the body and rotor motions were allowed to decay freely. The body pitch and roll modes were excited by deflecting the fuselage with pulley-mounted cords and then quickly releasing it.

The blade root flexures are shown in the exploded view of Fig. 2. The lead-lag flexure is fastened to a base and ring that allows the lead-lag flexure to be rotated to any pitch angle, although for the cases discussed in this paper, the lead-lag flexure was always positioned upright. The lead-lag flexure, base, and ring are firmly fastened to the rotor hub. A pair of side beams is connected to the outer part of the lead-lag flexure; these carry the load back toward the hub. The flap flexure is fastened to the inner edge of the side beams and in this way the lead-lag and flap flexure centerlines are made coincident. A blade root socket is fastened to the outer portion of the flap flexure and blade pitch angle changes are made at this point. Instead of the straight lead-lag flexure, the skewed lead-lag flexure that is shown in the inset of Fig. 2 is used to provide negative pitch-lag coupling (Case 3). The major rotor properties are shown in Table 1.

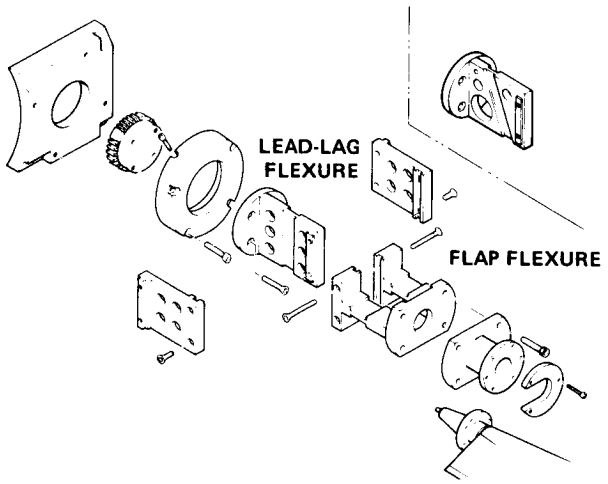

Fig. 2 Exploded view of blade root flexures.

Table 1 Model Rotor Properties

Property	Value
Rotor radius, R, in.	31.92
Blade chord, c, in.	1.65
Solidity, σ	0.0493
Hinge offset, e/R	0.105
Lock number, γ	7.37

The rotor flap and lead-lag flexures were strain-gaged as were the gimbal flexural pivots. The measured flexural strains were digitized and acquired on a digital computer. The rotating system data were transformed to the fixed system using the multiblade transform and the frequency and damping data were obtained from the rotor cyclic and body modes using the moving-block analysis.[2] A complete discussion of the model properties is provided in Appendix A. The measured modal damping and frequency used for the correlation is tabulated in Appendix B.

Correlation

Three cases were used for correlation. These cases differed only in the degree of aeroelastic coupling in the rotor as determined by blade pitch angle and pitch-lag coupling. The differences in the three cases are shown in Table 2.

Table 2 Correlation Cases

Case	Blade Pitch Angle, deg	Pitch-Lag Coupling
1	0	0
2	9	0
3	9	-0.4

Case 1

Modal Frequencies. This case examined modal damping and frequency for an uncoupled rotor configuration with the blade pitch set to zero degrees. Damping and frequency of the regressing lead-lag, body pitch, and body roll modes were obtained for rotor speeds from 0 to 950 rpm. Figure 3 shows individual comparisons of the fixed-system modal frequencies with nine different predictions. An understanding of the system behavior may be obtained by examining a typical prediction such as that done with DRAV21 as shown in Fig. 3a. The regressing lead-lag mode starts at about 6.6 Hz for nonrotating conditions and as rotor speed is increased, the fixed system modal frequency drops until it becomes zero at about 450 rpm (in the rotating system this is a 1/rev resonance). At higher rotor speeds the regressing lead-lag mode frequency increases. For rotor speeds below 450 rpm, the dimensionless regressing lead-lag frequency is greater than one (stiff inplane) and the rotor is not susceptible to aeromechanical instability. For rotor speeds above 450 rpm the dimensionless, regressing lead-lag frequency is less than one (soft inplane) and the rotor is susceptible to aeromechanical instability as the regressing lead-lag mode couples with the body pitch or roll mode. The regressing flap mode is highly damped at rotor speeds above 100 rpm and does not couple with the regressing lead-lag mode as it did for the experiment discussed in Ref. 3. The progressing flap and lead-lag modes are widely separated in frequency for rotor speeds above 200 rpm and therefore do not influence the other modes.

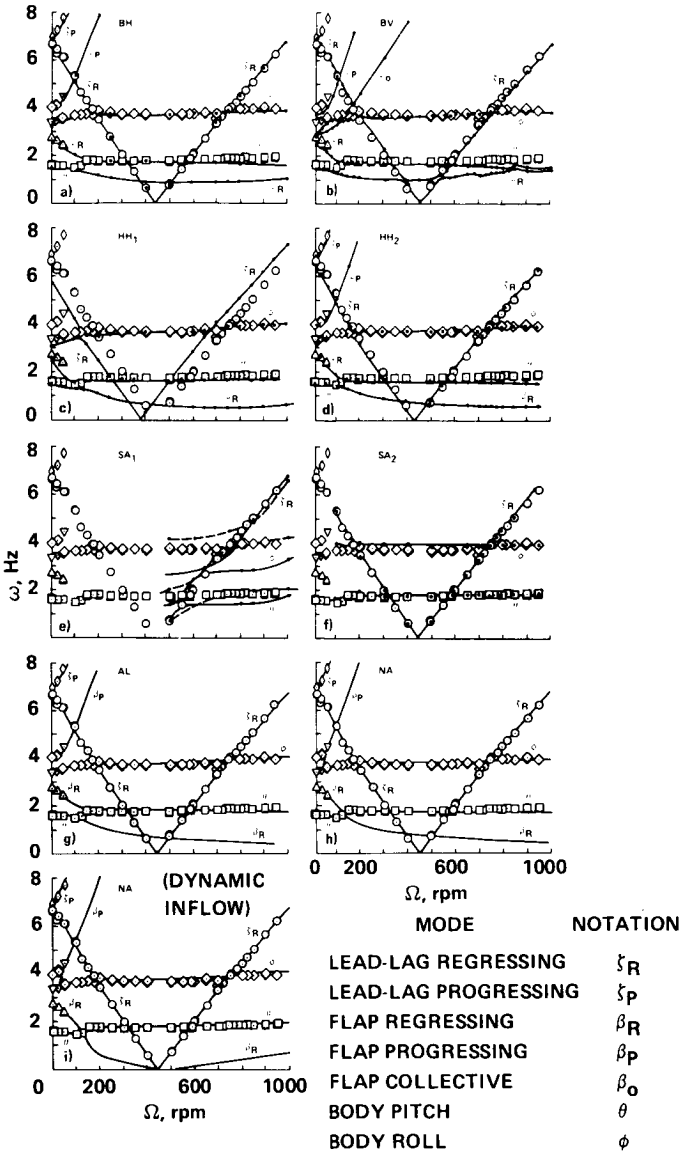

Fig. 3 Individual comparison of theory and experiment for Case 1 for fixed-system modal frequencies. a) DRAV21, Bell Helicopter Textron. b) C-90, Boeing Vertol. c) DART, Hughes Helicopters. d) E927-1, Hughes Helicopters. e) G400, Sikorsky Aircraft. Solid lines show calculations based on model properties. Dashed lines reflect change in properties to match rotating-body pitch and roll frequencies. f) E927-2, Sikorsky Aircraft. g) FLAIR, Aeromechanics Laboratory. h) CAMRAD, NASA Ames Research Center. i) CAMRAD with dynamic inflow, NASA Ames Research Center.

Most of the predictions in Fig. 3 show good to very good correlation (DRAV21, E927-1, FLAIR, and CAMRAD). The C-90 predictions show fair-to-good correlation, but exhibit some anomalous behavior. The C-90 program predicts that the collective flap mode couples with the body roll mode between 100 and 300 rpm. The mechanism for the coupling is not understood. At rotor speeds above 600 to 700 rpm, the C-90 predictions show apparent coupling between the regressing-flap and body-pitch modes (see also Fig. 5 below). This behavior appears spurious and suggests calculation problems with the code.

The DART correlation is considered to be only fair. This is largely because of the shift in lead-lag stiffness that resulted from using the mass and stiffness properties tabulated in Appendix A. These properties, which were calculated from detail drawings, predict a lower nonrotating frequency than was measured.

The G400 correlation was judged to be poor. The initial predictions using the documented model properties are shown as solid lines and do not match the measured body frequencies. Subsequently the uncoupled body pitch-and-roll frequencies were adjusted to provide a better match with the measurements; these results are shown as dashed lines. In either case the predicted frequencies indicate more coupling between the regressing lead-lag and body modes than was measured. An operational problem with G400 is the need to excite the appropriate modes in the time-history solution in order to estimate the frequency and damping from the transient decay. Considerable difficulty was encountered in exciting the body modes, particularly at the lower rotor speeds. The E927-2 correlation is considered to be fair. In general the correct behavior is shown, but the differences in the body roll mode and the absence of calculations at low rotor speeds degrade the correlation.

Regressing lead-lag mode damping. The damping of the regressing lead-lag mode for Case 1 is shown in Fig. 4. Calculations without dynamic inflow and with dynamic inflow are compared separately. The experimental measurements show a relatively constant level of damping except at the body roll mode crossing where the regressing lead-lag mode is unstable between 700 and 805 rpm. Most of the analyses show this same general behavior with the correlation ranging from fair for E927-2 and E927-3, fair-to-good for C-90, FLAIR, and CAMRAD, and good for DRAV21.

The DART analysis shows a range of instability that is much wider than the measurements and the correlation is considered to be poor. The center of instability is offset from the measured location and this is probably caused by the lead-lag frequency shift noted in Fig. 3. However, the greater range of instability that was calculated is probably caused by the inability to properly model the separate body pitch and roll frequencies with the isotropic representation used by DART. In addition, away from the body crossings DART predicts a damping level that is significantly below the rotor structural damping, and the mechanism for this destabilizing effect is unknown.

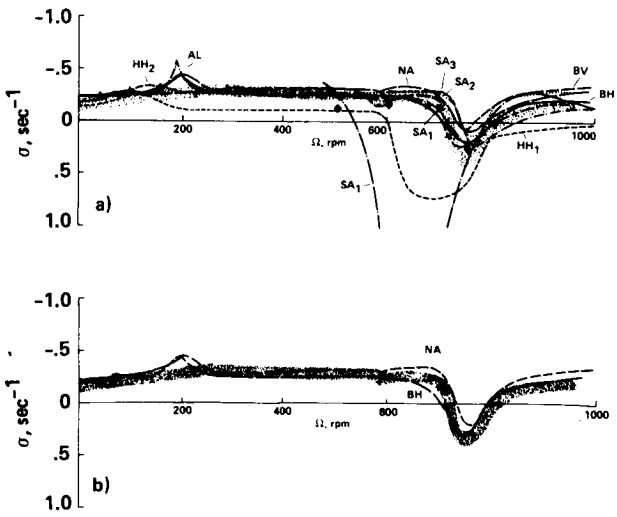

Fig. 4 Composite comparison of theory and experiment for Case 1 regressing lead-lag-mode damping. Data are shown by stippled area; analyses used are DRAV21 (BH), C-90 (BV), DART (HH_1), E927-1 (HH_2), G400 (SA_1, recalculations shown as diamond symbols), E927-2 (SA_2), E927-3 (SA_3), FLAIR (AL), and CAMRAD (NA). a) Without dynamic inflow. b) With dynamic inflow.

The G400 correlation is judged to be very poor and shows excessive sensitivity to body coupling effects. Following the initial Methodology Assessment, the G400 code was extensively revised. The correlation was significantly improved, as shown by the solid diamond symbols. However, the specific revisions that caused the improved predictive capability are not known.

Two of the prediction methods, DRAV21 and CAMRAD, have the option of predicting the stability with the inflow dynamics included. Although it is not completely clear from Fig. 4, the inclusion of dynamic inflow provided a minor improvement in the correlation for both of these analyses.

Body pitch mode damping. The body pitch-mode damping as a function of rotor speed is shown in Fig. 5. Theory and experiment show similar behavior with the damping rapidly increasing from its nonrotating value as the regressing flap and body pitch modes become strongly coupled between 100 and 150 rpm and then decreasing as the modes separate. Above 200 rpm there is a gradual increase in damping with rotor speed. Although similar behavior is seen in both the theoretical calculations and experimental results, the predicted level of damping from theory is significantly higher than the measurements for rotor speeds above 200 rpm. These differences are largely due to the rotor aerodynamics as the gimbal damping is very low, as can be seen by examining the zero rotor speed case. If dynamic inflow is included in the analytical model, better agreement is obtained with the experiment, as is shown in Fig. 5b.

In general, the correlation is considered poor-to-fair for the models without dynamic inflow, and fair-to-good and good for the models with dynamic inflow. The C-90 analysis is judged as poor because of the high damping level and anomalous damping increases at 675 and 850 rpm. These damping increases or bumps are not related to any frequency crossing or resonance and the lack of a physical explanation suggests that they are caused by code problems. The wobble in body pitch and flap regressing mode frequencies noted earlier appears to be related to this problem.

The G400 correlation was judged as poor. This is largely caused by the inability of the analysis to estimate the body mode damping at rotor speeds below 800 rpm. The E927-2 analysis in many ways shows the best agreement with the data, but its somewhat erratic behavior and lack of definition of

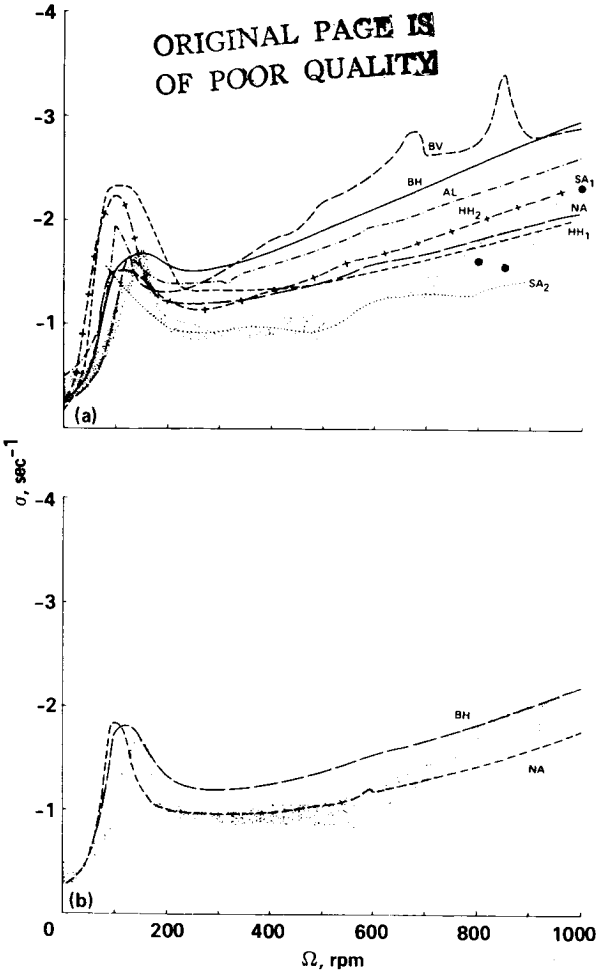

Fig. 5 Composite comparison of theory and experiment for Case 1 body pitch-mode damping. Data are shown by stippled area; analyses used are DRAV21 (BH), C-90 (BV), DART (HH_1), E927-1 (HH_2), G400 (SA_1, 3 points), E927-2 (SA_2), FLAIR (AL), and CAMRAD (NA). a) Without dynamic inflow. b) With dynamic inflow.

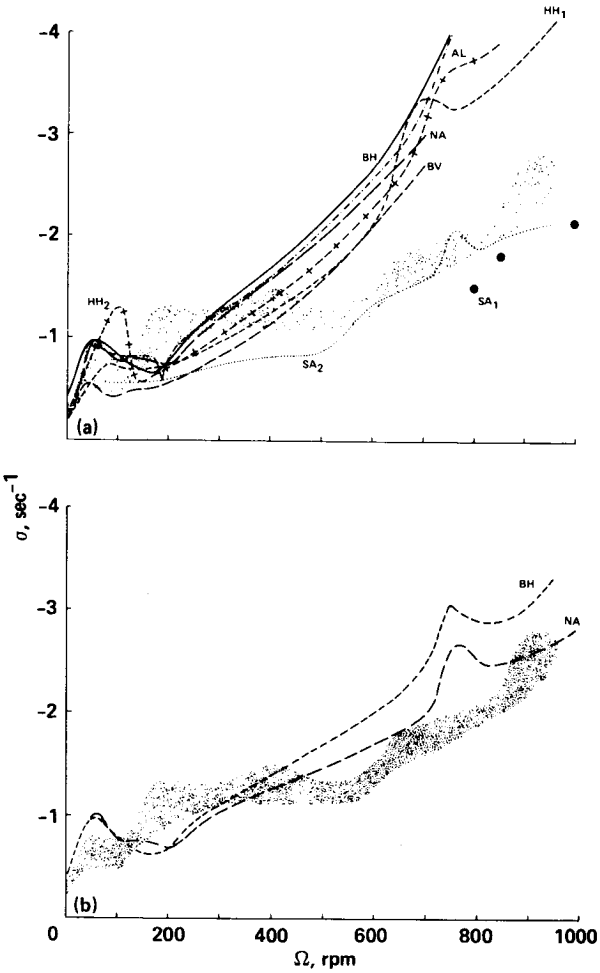

Fig. 6 Composite comparison of theory and experiment for Case 1 body roll-mode damping. Data are shown by stippled area; analyses used are DRAV21 (BH), C-90 (BV), DART (HH_1), E927-1 (HH_2), G400 (SA_1, 3 points), E927-2 (SA_2), FLAIR (AL), and CAMRAD (NA). a) Without dynamic inflow. b) With dynamic inflow.

the damping increase caused by coupling of the flap-regressing and body-pitch modes led to a judgment of poor-to-fair correlation.

Body roll-mode damping. The body roll-mode damping as a function of rotor speed is shown in Fig. 6. The experimental data show a somewhat larger increase in damping with rotor speed than in the body pitch case. However, there is no clear indication of a damping increase caused by coupling of the body roll mode with the progressing flap or regressing lead-lag modes at low rotor speeds. Note that roll-mode damping data were not obtained from 700 to 825 rpm because of the regressing lead-lag mode instability.

The theoretical predictions without dynamic inflow show a very similar increase in damping for rotor speeds above 200 rpm, and the increase is clearly greater than that seen in the experimental data. However, if dynamic inflow is included, the theory and experiment show much better agreement. The improvement in correlation that is achieved with dynamic inflow is more apparent in this case than for the body pitch mode shown in Fig. 5.

The analyses without dynamic inflow in general show only poor-to-fair correlation with the data. The damping predictions that include dynamic inflow show better agreement; the DRAV21 predictions are judged fair and the CAMRAD predictions fair-to-good. The Sikorsky E927-2 predictions are considered to be fair and would probably be judged better except for the somewhat erratic behavior that is shown. The G400 results are again considered to be poor, in part because of the inability to obtain damping estimates at lower rotor speeds.

Case 2

Individual comparisons of theory and experiment for the regressing lead-lag mode damping are shown in Fig. 7 as a function of rotor speed. The only difference between this case and Case 1 is that the blade pitch angle is set to 9° instead of 0°. The effect of this change is to couple the blade flap and lead-lag degrees of freedom and this has a strong effect upon the regressing lead-lag mode damping as can be seen by comparing this figure with Fig. 4. The destabilizing effect caused by coupling of the regressing lead-lag mode and the body pitch mode at 600 rpm is now evident, and the instability caused by coupling of the regressing lead-lag and body roll modes has deepened (0.7 sec^{-1} compared to 0.3 sec^{-1}) and broadened (150 rpm compared to 90 rpm).

The DRAV21, C-90, and FLAIR analyses all show fair correlation. The DRAV21 predictions show better agreement in the vicinity of the pitch mode, while C-90 and FLAIR show better agreement near the roll mode. However, in each case there remain areas of disagreement. Note also that for the DRAV21 calculations the effect of dynamic inflow is slight.

The E927-3 predictions in Fig. 7g show fair-to-good agreement with the data, with the only discrepancy being the inability to predict the measured recovery in damping at high rotor speeds. This case and the Case 1 regressing lead-lag mode damping are the only cases in the correlation effort in which all three E927 versions were used. For Case 1 only slight differences are seen between the three versions, but in the present case significant differences are evidenced. The public domain version, E927-1, shows a frequency shift and predicts too great an instability, while E927-2 shows only a slight instability. Both show only poor or poor-to-fair correlation with the data. The major differences in coding between the three versions has to do with the representation of the torsion degree of freedom. The E927-1 version includes only a rigid torsion degree of freedom; E927-2 adds a flexible torsion degree of freedom, but deletes some of the higher-order terms; and E927-3 retains all the higher-order terms. These differing representations have a major influence on the stability predictions even though the model rotor's first-torsion degree of freedom is greater than 20/rev based on nonrotating measurements. The sensitivity of the predictive capability to the modeling assumptions in this case suggests fundamental weaknesses in the E927 family of codes.

The DART analysis shows an excessive degree of instability and the correlation is considered poor. In part, this is caused by the frequency shift in the lead-lag degree of freedom discussed previously. However, even a shift of 50 rpm would not significantly improve the correlation.

The initial G400 calculations show very poor agreement with the data. From the three calculated values provided for the updated analysis (solid

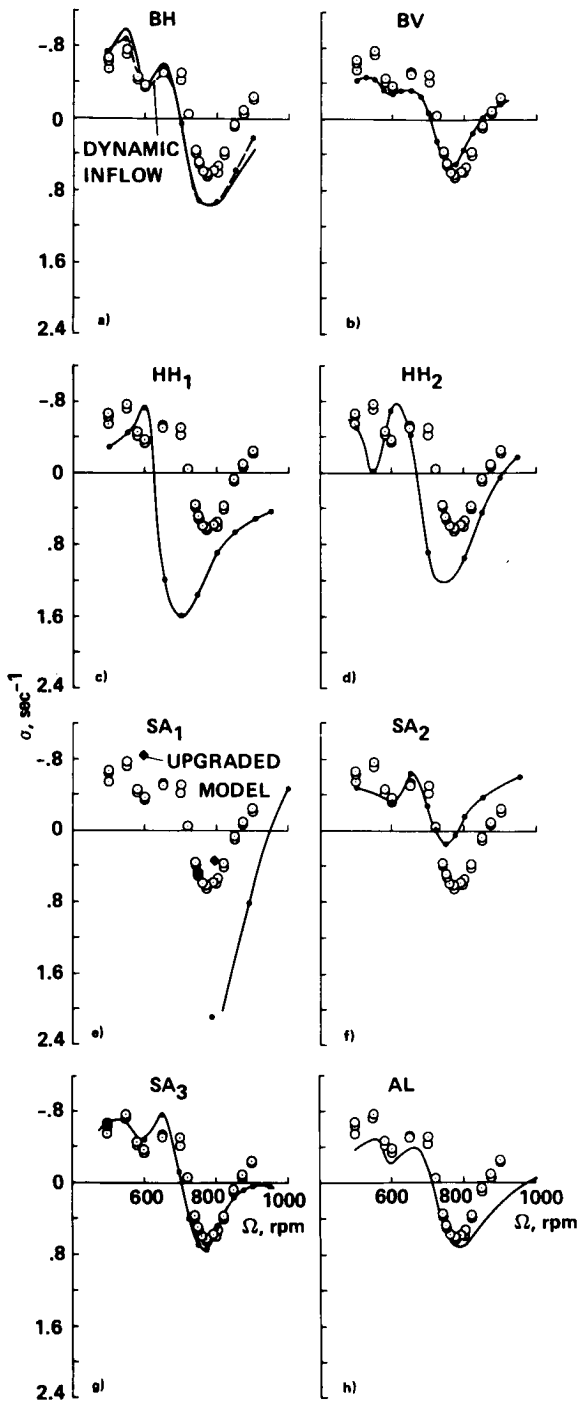

Fig. 7 Individual comparison of theory and experiment for Case 2 for regressing lead-lag-mode damping. a) DRAV21, Bell Helicopter Textron. b) C-90, Boeing Vertol. c) DART, Hughes Helicopters, d) E927-1, Hughes Helicopters. e) G400, Sikorsky Aircraft. f) E927-2, Sikorsky Aircraft. g) E927-3, Sikorsky Aircraft. h) FLAIR, Aeromechanics Laboratory.

diamonds in Fig. 7e), it appears that these problems are largely resolved. However, the number of calculated points using the updated model is too limited to adequately assess the improvement in the analysis capabilities.

Case 3

Individual comparisons of theory and experiment for the regressing lead-lag mode damping are shown in Fig. 8 as a function of the rotor speed for Case 3. The only difference between this case and Case 2 is the addition of negative pitch-lag coupling. Based on isolated blade stability theory,[4] the expected effect of the negative pitch-lag coupling would be to strongly stabilize the regressing lead-lag mode. This in fact occurs away from the body pitch- and roll-mode frequency crossings. For instance, the damping at 550 and 650 rpm is essentially doubled from Case 2 to Case 3. However, at the frequency crossings or "resonant" points, there is essentially no change in the damping.

The DRAV21 and FLAIR analyses show good agreement with the experimental measurements. The agreement for both analyses is improved over that obtained in Case 2, which is interesting in that Case 3 is considered a more difficult case to accurately analyze. As in Case 2, when dynamic inflow is included in the DRAV21 analysis, there are no significant changes in the regressing lead-lag damping.

The C-90 code shows fair agreement with the data. It correctly identifies the minimum stability points, but not the range of damping that is seen in the data. The two versions of E927 evidence difficulty in identifying the rotor speed for minimum stability. The E927-1 correlation is considered very poor-to-poor and does not predict instability, while E927-3 does show reasonably correct damping levels, but the correlation is judged poor-to-fair. The DART analysis shows excessive changes in damping, a substantial frequency shift in the minimum damping point, and an overly broad region of instability. The agreement with the measurements is considered poor.

Conservatism in Prediction of Stability

The potentially destructive nature of rotor instabilities has always been a major concern of the rotorcraft dynamics community. There is agreement that the long term goal in rotorcraft dynamics must be to obtain accurate predictions of rotorcraft stability. However, in the short term, there is a general belief that if the theoretical predictions are "conservative," that is, if they predict less stability than is measured, then they are suitable for design use. Such a feeling or belief ignores the ambiguity that exists whenever theory and experiment are compared and a difference is obtained. Is the difference due to the theory or the experiment? If it is due to some limitation of the modeling assumptions, then can any prediction be called conservative if that limitation is unknown? An example is selected from the correlation effort reported here. Figure 9 compares the

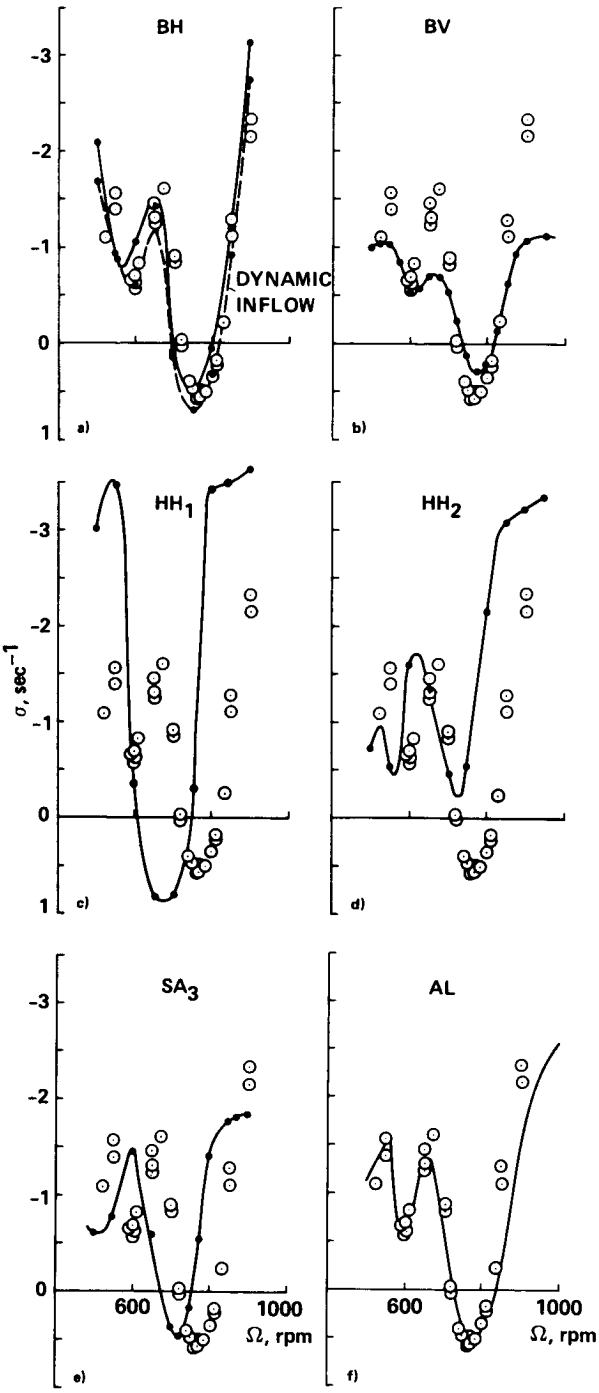

Fig. 8 Individual comparison of theory and experiment for Case 3 for regressing lead-lag mode damping. a) DRAV21, Bell Helicopter Textron. b) C-90, Boeing Vertol. c) DART, Hughes Helicopters, d) E927-1, Hughes Helicopters. e) E927-3, Sikorsky Aircraft. f) FLAIR, Aeromechanics Laboratory.

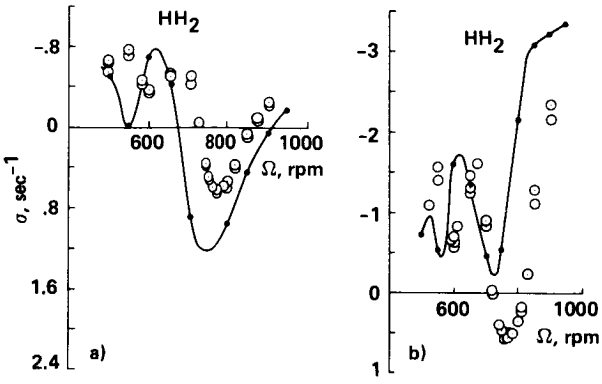

Fig. 9 Comparison of E927-1 predictions for Cases 2 and 3. a) Case 2, 9° blade pitch angle, no pitch-lag coupling. b) Case 3, 9° blade pitch angle, -0.4 pitch-lag coupling.

E927-1 predictions of regressing lead-lag mode damping for Cases 2 and 3. The only difference between the two cases is the addition of negative pitch-lag coupling in Case 3. As discussed earlier, the correlation in Case 2 is judged poor-to-fair. However, the prediction can be considered conservative in the sense that it shows less stability in general than is measured. Yet, as shown in Fig. 9b, the addition of pitch-lag coupling changes this picture. The analysis is now unconservative and predicts no instability where one was obtained in the experiment. The lack of correlation between theory and measurement represents an element of risk in the application of a theoretical model. The use of terms such as "conservative prediction" or "correct trends" unfortunately obscure this element of risk.

Conclusions

Nine analyses were compared with one or more cases selected from an experiment that measured the frequency and damping of a model rotor in hover for different conditions of rotor coupling.

1) The DRAV21 analysis used by Bell Helicopter Textron was considered to give fair-to-good correlation for the three cases.

2) The C-90 analysis used by Boeing Vertol was judged to have fair correlation overall.

3) Two analysis codes were used by Hughes Helicopter. Their DART analysis was considered to provide poor-to-fair correlation and their E927-1 code was judged fair overall.

4) Sikorsky Aircraft used the analysis code G400 and two versions of E927: E927-2 and E927-3. None of these codes was used for all cases. Overall, G400 was judged to be very poor-to-poor although a limited number of more recent calculations have shown substantial improvement. For the cases considered, E927-2 was considered poor-to-fair, while E927-3 showed better performance and was judged fair.

5) The FLAIR analysis of the U.S. Army Aeromechanics Laboratory was considered to provide fair-to-good correlation.

6) The NASA Ames CAMRAD calculations were made for one case and were judged to be good for this case.

Two of the nine analyses predicted damping and frequency with and without dynamic inflow. The effect of dynamic inflow was to significantly improve the agreement for the body mode damping of Case 1, but regressing lead-lag mode damping was only slightly affected by dynamic inflow.

References

[1]Bousman, William G., "An Experimental Investigation of the Effects of Aeroelastic Couplings on Aeromechanical Stability of a Hingeless Rotor Helicopter," Journal of the American Helicopter Society, Vol. 26, No. 1, Jan. 1981, pp. 46-54.

[2]Bousman, William G. and Winkler, Diana J., "Application of the Moving-Block Analysis," 22nd Structures, Structural Dynamics and Materials Conference Proceedings (Part 2), Apr. 1981, pp. 755-763.

[3]Bousman, William G., "A Comparison of Theory and Experiment for Coupled Rotor-Body Stability of a Hingeless Rotor Model in Hover Under Simulated Vacuum Conditions," NASA CP-10007, May 1988.

[4]Ormiston, R. A. and Hodges, D. H., "Linear Flap-Lag Dynamics of Hingeless Helicopter Rotor Blades in Hover," Journal of the American Helicopter Society, Vol. 17, No. 2, Apr. 1972, pp. 2-14.

[5]Bousman, W. G., Sharpe, D. L., and Ormiston, R. A., "An Experimental Study of Techniques for Increasing the Lead-Lag Damping of Soft Inplane Hingeless Rotors," Preprint No. 1035, American Helicopter Society 32nd Annual National Forum, May 1976.

[6]Silcox, H. F., "Analytical and Model Investigation of Hingeless Rotor Air Statility, Volume 1, Section A: Structural Analysis--Rigid Blades," Rep. No. D210-10475-1A, Boeing Company, 1972.

[7]Bousman, William G., "An Experimental Investigation of Hingeless Helicopter Rotor-Body Stability in Hover," NASA TM-78489, June 1978.

Appendix A--Model Properties

The three cases examined in this paper are from an experiment originally reported in Ref. 1. The experimental model properties in this appendix are taken from that reference with the exception of the tabulated mass and stiffness properties in Tables 3 to 6 which have not been reported

Table 3 Calculated Mass and Stiffness Properties of Lead-Lag Flexure[a]

BLADE STATION in.	WEIGHT $lb_m/in.$	EI_f 10^6 lb-in^2	EI_c 10^6 lb-in^2	GJ 10^6 lb-in^2	I_θ lb_m-in^2/in.
2.431	0.422	5.18	5.18	3.93	0.101
2.581	0.422	5.18	5.18	3.93	0.101
2.581	0.0682	1.11	0.179	0.116	0.0110
2.750	0.0682	1.11	0.179	0.116	0.0110
2.791	0.0398	0.756	0.0102	0.116	0.0110
2.890	0.0266	0.597	0.00701	0.116	0.0110
2.989	0.0398	0.756	0.0102	0.116	0.0110
3.030	0.0682	1.11	0.0179	0.116	0.0110
3.200	0.0682	1.11	0.0179	0.116	0.0110
3.200	0.0292	0.477	0.00141	0.00139	0.00155
3.225	0.0097	0.159	0.0000521	0.00139	0.00155
3.450	0.0097	0.159	0.0000521	0.00139	0.00155
3.475	0.0292	0.477	0.00141	0.00139	0.00155
3.475	0.0682	1.11	0.0179	0.114	0.0110
3.553	0.0682	1.11	0.0179	0.114	0.0110
3.585	0.0451	0.857	0.0118	0.114	0.0110
3.663	0.0357	0.745	0.00935	0.114	0.0110
3.741	0.0451	0.857	0.0118	0.114	0.0110
3.773	0.0682	1.11	0.0179	0.114	0.0110
4.101	0.0682	1.11	0.0179	0.114	0.0110

a MAT'L – 17-4 PH STAINLESS; $\rho = 0.282\ lb_m/in^3$, $E = 29 \times 10^6\ lb/in^2$, $G = 11 \times 10^6\ lb/in^2$.
b AXIS OF SYMMETRY COINCIDENT WITH 0.25c

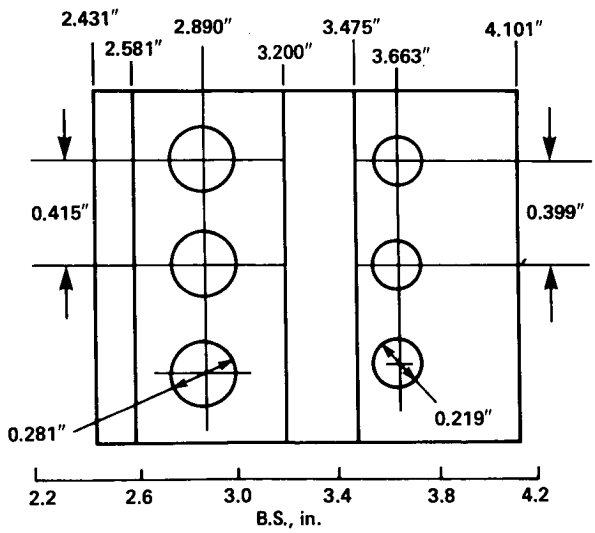

LEAD-LAG FLEXURE

Table 4 Calculated Mass and Stiffness Properties of Side Beams[a]

BLADE STATION in.	WEIGHT lb_m/in.	EI_f 10^6 lb-in^2	EI_c 10^6 lb-in^2	GJ 10^6 lb-in^2	I_θ lb_m in^2/in.
2.633	0.0535	0.468	0.298	0.0109	0.0105
2.883	0.0535	0.468	0.298	0.0109	0.0105
2.883	0.0410	0.359	0.190	0.0109	0.00493
2.983	0.0410	0.359	0.190	0.0109	0.00493
3.029	0.0234	0.269	0.109	0.0109	0.00493
3.139	0.0160	0.221	0.0745	0.0109	0.00493
3.249	0.0234	0.269	0.109	0.0109	0.00493
3.295	0.0410	0.359	0.190	0.0109	0.00493
3.439	0.0410	0.359	0.190	0.0109	0.00493
3.485	0.0234	0.269	0.109	0.0109	0.00493
3.595	0.0160	0.221	0.0745	0.0109	0.00493
3.705	0.0234	0.269	0.109	0.0109	0.00493
3.751	0.0410	0.359	0.190	0.0109	0.00493
3.851	0.0410	0.359	0.190	0.0109	0.00493
3.851	0.0613	0.537	0.220	0.0109	0.00957
4.101	0.0613	0.537	0.220	0.0109	0.00957

a MAT'L – Ti-6Al-4V ALLOY; ρ = 0.160 lb_m/in^3, E = 16 × 10^6 lb/in^2, G = 6.2 × 10^6 lb/in^2.

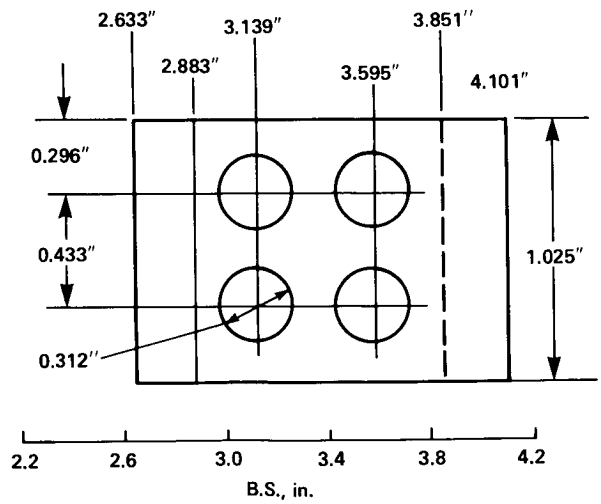

SIDE BEAMS

Table 5 Calculated Mass and Stiffness Properties of Flap Flexure[a]

BLADE STATION in.	WEIGHT $lb_m/in.$	EI_f 10^6 lb-in^2	EI_c 10^6 lb-in^2	GJ 10^6 lb-in^2	I_θ lb_m in^2/in.
2.633	0.276	2.49	9.20	9.92	0.114
2.883	0.276	2.49	9.20	9.92	0.114
2.883	0.0510	0.0156	1.70	1.46	0.0167
3.088	0.0510	0.0156	1.70	1.46	0.0167
3.088	0.0186	0.000759	0.621	0.0192	0.00106
3.111	0.0062	0.000028	0.207	0.0192	0.00106
3.588	0.0062	0.000028	0.207	0.0192	0.00106
3.611	0.0186	0.000759	0.621	0.0192	0.00106
3.611	0.510	0.0156	1.70	0.185	0.0167
4.223	0.510	0.0156	1.70	0.185	0.0167
4.223	0.242	2.00	0.763	3.98	0.0839
4.298	0.242	2.00	0.763	3.98	0.0839
4.298	0.368	3.54	6.62	3.98	0.0988
4.423	0.368	3.54	6.62	3.98	0.0988

a MAT'L – 17-4 pH STAINLESS: $\rho = 0.282\ lb/in^3$, $E = 29 \times 10^6\ lb/in^2$, $G = 11 \times 10^6\ lb_f/in^2$. AXIS OF SYMMETRY COINCIDENT WITH 0.25c.

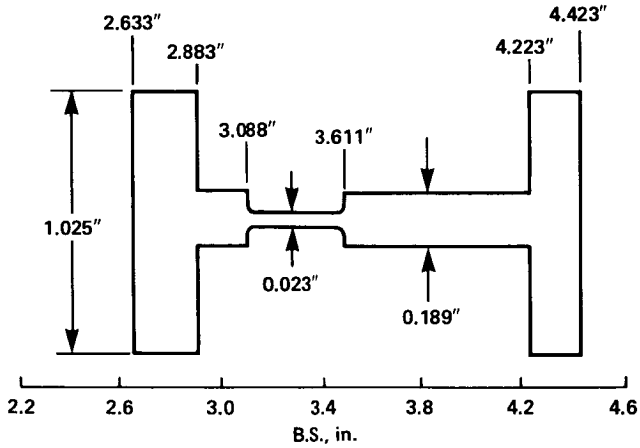

FLAP FLEXURE

Table 6 Calculated Mass and Stiffness Properties of Hub Flexure and Blade

Blade Station, in.	Weight, lb_m/in.	EI_f, 10^6 lb-in.^{2}	EI_c, 10^6 lb-in.^{2}	GJ, 10^6 lb-in.^{2}	I_θ, lb_m in.^{2}/in.
2.034	0.573	20.1	20.1	15.6	0.403
2.431	0.573	20.1	20.1	15.6	0.403
2.431	0.422	5.18	5.18	3.93	0.101
2.581	0.422	5.18	5.18	3.93	0.101
2.581	0.0533	1.11	0.0179	3.93	0.101
2.633	0.0533	1.11	0.0179	3.93	0.101
2.633	0.398	0.291	0.0169	0.00995	0.136
2.750	0.398	0.291	0.0169	0.00995	0.136
2.791	0.369	0.259	0.00985	0.00995	0.136
2.883	0.357	0.239	0.00706	0.00995	0.136
2.883	0.120	0.0146	0.00695	0.00990	0.0326
2.890	0.119	0.0146	0.00673	0.00990	0.0326
2.983	0.131	0.0147	0.00945	0.00990	0.0326
2.989	0.131	0.0147	0.00962	0.00990	0.0326
3.030	0.143	0.0146	0.0152	0.00990	0.0326
3.088	0.139	0.0145	0.0148	0.00990	0.0326
3.088	0.106	0.000756	0.0146	0.00656	0.0170
3.111	0.0923	0.000028	0.0138	0.00656	0.0170
3.139	0.0904	0.000028	0.0135	0.00656	0.0170
3.200	0.0945	0.000028	0.0140	0.00656	0.0170
3.200	0.0555	0.000028	0.00138	0.00116	0.00754
3.225	0.0377	0.000028	0.000052	0.00116	0.00754
3.249	0.0393	0.000028	0.000052	0.00116	0.00754
3.295	0.0569	0.000028	0.000052	0.00116	0.00754
3.439	0.0569	0.000028	0.000052	0.00116	0.00754
3.450	0.0527	0.000028	0.000052	0.00116	0.00754
3.475	0.0626	0.000028	0.00139	0.00116	0.00754
3.475	0.102	0.000028	0.0146	0.00655	0.0170
3.485	0.0978	0.000028	0.0143	0.00655	0.0170
3.553	0.0932	0.000028	0.0142	0.00655	0.0170
3.585	0.0680	0.000028	0.00976	0.00655	0.0170
3.588	0.0674	0.000028	0.00968	0.00655	0.0170
3.595	0.0699	0.000250	0.00967	0.00655	0.0170
3.611	0.0777	0.000756	0.00952	0.00655	0.0170
3.611	0.110	0.0143	0.00961	0.00944	0.0326
3.663	0.107	0.0144	0.00848	0.00944	0.0326
3.705	0.115	0.0145	0.00969	0.00944	0.0326
3.741	0.133	0.0146	0.0110	0.00944	0.0326
3.751	0.144	0.0147	0.0127	0.00944	0.0326
3.773	0.160	0.0148	0.0162	0.00944	0.0326
3.851	0.160	0.0148	0.0162	0.00944	0.0326
3.851	0.181	0.0150	0.0164	0.00944	0.0373
4.101	0.181	0.0150	0.0164	0.00944	0.0373
4.101	0.051	0.0156	1.70	0.185	0.0167
4.223	0.051	0.0156	1.70	0.185	0.0167
4.223	0.222	1.77	3.66	2.18	0.0550
4.484	0.220	1.77	3.66	2.18	0.0550
4.484	0.231	1.77	3.66	2.18	0.0550
4.613	0.231	1.77	3.66	2.18	0.0550
4.613	0.0529	1.24	1.24	0.0959	0.00247
5.078	0.0510	1.24	1.24	0.0959	0.00243
5.260	0.191	1.24	1.24	0.0959	0.0394
5.410	0.191	1.24	1.24	0.0959	0.0394
5.410	0.0243	0.0459	0.0459	0.0238	0.000728
5.469	0.0291	0.0538	0.0538	0.0288	0.000867
5.469	0.119	0.0538	0.0538	0.0288	0.0147
5.529	0.118	0.0991	0.0991	0.0616	0.0155
5.529	0.155	0.0991	0.0991	0.0616	0.0295
5.659	0.160	0.101	0.101	0.0596	0.0297
5.659	0.0447	0.101	0.101	0.0596	0.00172
5.764	0.0470	0.102	0.102	0.0568	0.00167
5.764	0.0332	0.0526	0.0526	0.0187	0.000684
5.924	0.00763	0.00228	0.0617	0.0012	0.000711
7.924	0.00758	0.00228	0.0617	0.0012	0.000869
31.924	0.00758	0.00228	0.0617	0.0012	0.000869

before. In a few cases, errors have been found in the Ref. 1 model properties, and these are corrected here.

Rotor Properties

Geometric Properties. The major rotor geometric properties have been tabulated in Table 1. Section lift and drag coefficient data for these blades have been calculated from steady bending-moment data obtained in a previous experiment.[5] Analytic functions that provide a good fit to these data are

$$c_\ell = 0.15 + 5.73\alpha$$

$$c_d = 0.0079 + 1.7\alpha^2$$

where c_ℓ is the section lift coefficient, α is the section angle of attack in radians, and c_d is the section drag coefficient. The camber of the NACA 23012 profile provides a section lift coefficient of 0.15 at zero pitch angle. A value for the section pitching moment, c_{mo}, of -0.012 is assumed.

Mass and Stiffness Properties. The design drawings of the hub were used to calculate mass, stiffness, and pitching inertias outboard of blade station 2.034 in. This blade station is the outer face of the leftmost part in the exploded view shown in Fig. 2. The mass, stiffness, and pitching inertias of the blade were obtained from Ref. 6. Properties are tabulated separately for the lead-lag flexure, side beams, and flap flexure in Tables 3 to 5. Table 6 provides the composite properties for these components as well as the blade and blade root properties outboard of B.S. 4.423 in. Running weight and pitch inertia were assumed to be additive in this table and the combined stiffness was based on a series spring representation.

Measurements were made of the mass, mass centroid, and moment of inertia for three flap-flexure blade combinations; the mean values are shown in Table 7. These measurements were adjusted or corrected to subtract the effect of the flap flexure inboard of the flap flexure centerline (B.S. 3.350 in.) and to add the contribution of the lead-lag flexure and side beams. The mass properties of the blade and hub outboard of the flap flexure centerline were calculated from Table 6 and are shown in Table 7. The difference that is seen in the blade mass is substantially greater than the differences between the three blades (±0.6%); the reasons for this are unknown. However, the calculations for the mass centroid and the moment of inertia show good agreement between the adjusted measurements, and the calculation and the difference is within the blade-to-blade variation.

There are some small differences between the mass properties of Table 7 and Table 2 of Ref. 1. In Ref. 1 the mass, centroid, and moment of inertia are defined for the blade and flap flexure outboard of the flap flexure centerline (B.S. 3.350 in.). The definition used here is based on all hub parts outboard of B.S. 3.350 in. and this includes portions of the side beams and lead-lag flexure. The calculation for rotor polar inertia used here is based on the mass properties of Table 6 and is lower than the Ref. 1 value which is considered inaccurate.

Modal Frequency and Damping. The flexure/blade combinations were removed from the model at B.S. 2.034 in. and their frequency and damping were determined individually. Mean values for three measurements are shown in Table 8. The frequencies calculated using this simple flexure and inertia representation do not account for flexibility in the blade. This flexibility will further reduce the calculated frequency, an effect that can be approximated by using the elastic coupling parameter, R.

$$\omega = \sqrt{(1 - R)}\omega_{flexure}$$

Values for R were determined in Ref. 5 from non-rotating measurements

Table 7 Hub and Blade Mass Properties

Quantity	Measured	Adjusted[a]	Calculated	Error[b]
Mass, lb_m	0.5356	0.5324	0.5199	-2.4%
Centroid of mass with respect to hub center, in.	9.562	10.01	9.984	-0.3%
Flapping and lead-lag moment of inertia with respect to B.S. 3.35 in., lb_m-$in.^2$	59.01	58.40	59.48	+1.9%
Pitch inertial, lb_m-$in.^2$	--	--	0.0898	--
Rotor polar inertia, lb_m-$in.^2$	--	--	275.3	--

[a]Flap flexure effect inboard of B.S. 3.35 in. removed (Table); effects of lead-lag flexure (Table 3) and side beams (Table 4) added.
[b]Based on adjusted measurement.

Table 8 Modal Frequency and Damping

Case	Mode	Measured Frequency, Hz	Calculated Frequency, Hz[a]	Error, %	Measured Damping, %
1,2	First flap	3.14	3.11	-1.0	--
	Second flap	32.20	--	--	0.49
	First lead-lag	6.70	6.17	-7.9	0.52
3	First flap	3.13	--	--	--
	First lead-lag	7.16	--	--	0.65

[a] $\omega = \sqrt{K/I_o}$, where $K = EI/\ell$ and is based on flexure only; I_o is from Table 7.

$R = 0.123$ for Cases 1 and 2

$R = 0.121$ for Case 3

These values produce calculated frequencies of 7.3% and 13.8% below the measurements for flap and lead-lag, respectively. This comparison suggests that the flap and chord stiffnesses tabulated in Table 6 are too low and need to be increased to properly match the measured nonrotating frequencies.

The higher blade mode-frequencies have been measured and reported in Ref. 7. The measured third flap-mode frequency was 96 Hz; the second and third lead-lag frequencies were 150 and 357 Hz, respectively; and the first torsion frequency was 342 Hz.

Body Properties

Geometric Properties. The distance from the gimbal center to the rotor plane was calculated from design drawings and is 9.470 in.

Mass and Stiffness Properties. Mass, inertia, and stiffness measurements were made on the model with the blade/flexure combinations removed leaving only the adaptor plates. The mass of the body was determined by removing the body from the stand and weighing the model with roll-axis gimbal plates attached. Separate measurements were made of the pitch-axis gimbal frame so that the measured weight could be referred to the roll axis (gimbal frame weight not included) or pitch axis (gimbal frame weight included).

The model was ballasted to locate the lateral and longitudinal c.g. positions at the gimbal center prior to weight and c.g. measurements. The vertical c.g. was determined by placing the model on its side supported by the roll flexure pivots and measuring the force required to balance the model about the gimbal center.

The model was reinstalled in the stand and connections for power, instrumentation, and so forth were made prior to making frequency measurements of the body in roll and pitch for a number of different gimbal-spring stiffnesses. The resulting frequencies are shown in Fig. 10 as a function of the square root of the effective spring stiffness. The body inertias were calculated assuming that the body acted as a single-degree-of-freedom oscillator. A linear regression fit was made to the data as shown. The spring stiffness was corrected for the offset of the model vertical c.g.

Mass and inertia measurements were adjusted to include the hub hardware inboard of B.S. 3.350 in. The measured and corrected properties are shown in Table 9 referred to both the roll and pitch axes. The data referred to the pitch axis include the effects of the gimbal frame.

Table 9 Body Mass and Inertia Properties

	Roll Axis		Pitch Axis	
	Measured	Adjusted	Measured	Adjusted
Body mass, slugs	1.26[a]	1.30	1.50[a]	1.55
Vertical c.g., in.	0.287[a]	0.574	0.241[a]	0.484
Inertia referenced to gimbal center, slug-in.^{2}	15.1	18.8	60.8	64.4

[a] Corrected for gimbal frame.

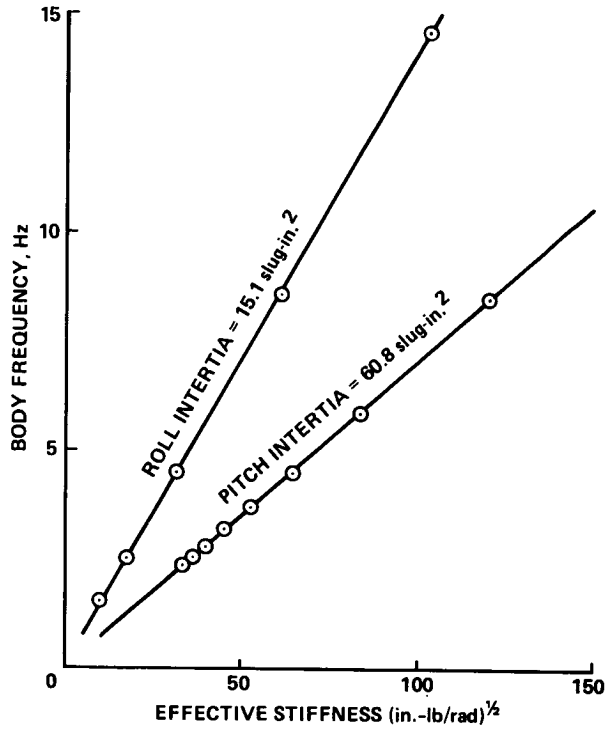

Fig. 10 Body frequency as a function of gimbal stiffness without rotor.

The stiffness of the model in roll was measured directly for the roll spring used during the experiment. The value obtained was

$$K_{\phi} = 985 \text{ in.-lb/rad}$$

Stiffness measurements in pitch were made with two cantilevered springs installed. However, during the experiment only one spring was used, so the stiffness may be estimated from the single-spring frequency measurements and the inertia of Table 9.

$$K_{\theta} = 725 \text{ in.-lb/rad}$$

Body Frequency and Damping. Measurements were made of the coupled rotor and body frequency and damping for all configurations reported in Ref. 1. Average values for body frequency and damping are

Roll: $\omega = 3.96$ Hz; $\zeta = 0.929\%$

Pitch: $\omega = 1.59$ Hz; $\zeta = 3.20\%$

Higher-mode stand frequencies were excited and measured to determine the frequency spacing with respect to the body modes. The next-higher stand frequencies were static mast--rolling and pitching at 46.0 and 45.5 Hz, respectively.

Appendix B--Experimental Data

Tables 10 through 13 give the measured rotor speed and modal frequencies and damping for Cases 1-3. For Case 1 it was possible to obtain the modal frequency and damping of the flapping modes and the progressing lead-lag mode for rotor speeds up to 50 rpm and these are given in Table 10. For Case 1 for rotor speeds above 50 rpm, modal damping and frequency were obtained for the regressing lead-lag, body pitch, and body roll modes as given in Table 11. The regressing lead-lag mode damping is shown in Tables 12 and 13 for Cases 2 and 3, respectively. These data were obtained from the experiment reported in Ref. 1. The modal frequencies and damping were measured in fixed system coordinates using the moving-block analysis[2] following a multiblade transformation from the rotating coordinates.

Appendix C--Correlation

All the theoretical predictions and experimental data for the selected cases are shown in this appendix in Figs. 11 to 21. In some cases figures from the main text are repeated here for completeness. Two formats are used for the correlation. The first format compares the theoretical predictions and experimental data individually for each mathematical model used. In this format the actual calculated points are shown as solid symbols. The curve between points was faired by the analyst involved. The data are shown as open symbols. The second format compares all the theoretical predictions on a single composite plot using the faired curve from the first format and the experimental data are shown as a stippled area. An exception to this second format is that no composite comparison is made of modal frequencies. A code is used to identify the theoretical predictions for both the individual and composite comparisons; it is explained in Table 14.

Table 10 Modal Frequencies and Damping from 0 to 50 rpm, Case 1

Ω, rpm	$\omega_{\zeta r}$, Hz	$\sigma_{\zeta r}$, sec^{-1}	$\omega_{\zeta p}$, Hz	$\sigma_{\zeta p}$, sec^{-1}	$\omega_{\beta r}$, Hz	$\sigma_{\beta r}$, sec^{-1}	$\omega_{\beta p}$, Hz	$\sigma_{\beta p}$, sec^{-1}	ω_{θ}, Hz	σ_{θ}, sec^{-1}	ω_{ϕ}, Hz	σ_{ϕ}, sec^{-1}
0	6.68	-0.184	6.94	-0.232	2.72	-0.176	3.42	-0.291	1.58	-0.323	3.95	-0.242
	6.68	-0.165	6.98	-0.152	2.72	-0.168	3.35	-0.518	1.61	-0.427	3.97	-0.284
	--	--	6.98	-0.186	--	--	3.36	-0.721	--	--	--	--
	--	--	6.94	-0.236	--	--	--	--	--	--	--	--
26	6.47	--	7.33	-0.306	2.59	-0.439	3.46	-0.756	1.58	-0.379	4.07	-0.470
	6.26	--	7.19	--	2.56	-0.426	3.37	-0.708	1.57	-0.352	4.07	-0.456
50	6.09	--	7.73	--	2.37	-0.915	4.47	--	1.56	-0.450	3.57	-0.747
	6.10	--	7.72	--	2.44	--	4.46	--	1.55	-0.443	3.53	-0.517
	--	--	7.62	--	2.47	-0.632	--	--	--	--	--	--
	--	--	--	--	2.43	-0.441	--	--	--	--	--	--

Table 11 Modal Frequencies and Damping from 100 to 950 rpm, Case 1, Continued

Ω, rpm	$\omega_{\zeta r}$, Hz	$\sigma_{\zeta r}$, sec^{-1}	ω_{θ}, Hz	σ_{θ}, sec^{-1}	ω_{ϕ}, Hz	σ_{ϕ}, sec^{-1}
100	5.30	--	1.48	-1.01	3.63	-0.498
	5.32	--	1.47	-1.11	3.64	-0.519
	5.24	--	--	--	--	--
	5.22	--	--	--	--	--
125	4.62	--	1.55	--	3.67	-0.734
	--	--	1.53	--	3.68	-0.770
150	4.28	--	1.77	-1.63	3.69	-0.780
	4.28	--	1.80	-1.69	3.67	-0.770
175	3.90	--	1.76	-1.05	3.66	--
	3.92	--	1.77	-1.07	3.66	-1.26
200	3.44	--	1.76	-1.05	3.78	--
	3.47	--	1.74	-1.02	3.79	--
	3.42	--	--	--	3.84	--
	3.45	--	--	--	3.86	--
250	2.74	-0.312	1.77	-0.890	3.73	--
	2.73	-0.311	1.74	-0.996	3.69	--
300	2.01	-0.301	1.77	-0.911	3.71	-1.20
	2.01	-0.310	1.73	-0.902	3.69	-1.22
350	1.30	-0.294	1.75	-0.881	3.70	-1.22
	1.29	-0.296	1.76	-0.958	3.67	-1.14
400	0.62	-0.273	1.76	-1.03	3.71	-1.45
	0.64	-0.295	1.74	-1.02	3.66	-1.31
500	0.75	-0.260	1.76	-0.921	3.63	-1.23
	0.74	-0.280	1.74	-0.942	3.65	-1.29
550	1.41	-0.279	1.79	-1.10	3.65	-1.26
	1.38	-0.285	1.76	-0.953	3.66	-1.31
	1.39	-0.282	1.75	-1.07	3.64	-1.20
	--	--	1.75	-1.05	3.64	-1.24
	--	--	1.76	-1.03	3.64	-1.21
580	1.77	-0.269	1.78	-0.876	3.65	-1.21
	1.80	-0.266	1.78	-0.905	3.65	-1.27
	--	--	1.78	-0.888	--	--
585	1.86	-0.227	1.82	-0.924	3.70	-1.36
	1.85	-0.239	1.81	-0.980	3.68	-1.39
	--	--	--	--	3.67	-1.34
600	2.01	-0.228	1.79	-1.27	3.71	-1.48
	2.04	-0.249	1.78	-1.22	3.69	-1.39
650	2.68	-0.249	1.81	-1.21	3.79	-1.78
	2.68	-0.255	1.82	-1.15	3.75	-1.63
700	3.31	-0.200	1.81	-1.33	3.75	-1.63
	3.33	-0.195	1.81	-1.43	3.64	--
720	3.59	-0.076	1.81	-1.52	--	--
	3.59	-0.009	1.81	-1.40	--	--
	3.59	-0.006	--	--	--	--
	3.57	-0.055	--	--	--	--
725	3.65	0.127	1.81	-1.53	--	--
740	3.80	0.325	1.87	-1.44	--	--
	3.80	0.313	1.84	-1.42	--	--
750	3.91	0.355	--	--	--	--
	3.86	0.363	--	--	--	--
	3.87	0.360	--	--	--	--
760	3.99	0.320	1.84	-1.56	--	--
	3.99	0.324	--	--	--	--
780	4.21	0.205	1.85	-1.51	--	--
	4.19	0.225	1.82	-1.59	--	--
	4.20	0.213	--	--	--	--
800	4.43	0.037	1.84	-1.73	3.94	--
	4.44	0.014	1.84	-1.73	3.93	--
	--	--	1.83	-1.77	--	--
820	4.70	-0.082	1.89	-1.52	3.95	-2.09
	4.70	-0.072	1.89	-1.52	3.95	-2.05
	4.69	-0.075	--	--	--	--
850	5.01	-0.107	1.86	-1.57	3.94	-2.06
	5.01	-0.126	1.84	-1.76	3.91	-2.20
	5.03	-0.125	--	--	--	--
	500	-0.125	--	--	--	--
900	5.64	-0.166	1.91	-2.09	4.00	-2.74
	5.64	-0.173	1.87	-2.09	3.97	-2.23
950	6.21	-0.175	1.90	-1.95	3.93	-2.71
	6.21	-0.169	1.93	-2.26	3.97	-2.52

Table 12 Regressing Lead-Lag Mode Damping, Case 2

Ω, rpm	$\sigma_{\zeta r_1}$ sec^{-1}
500	-0.666
500	-0.640
501	-0.553
549	-0.766
549	-0.721
580	-0.460
581	-0.431
600	-0.353
600	-0.373
650	-0.507
651	-0.537
700	-0.502
701	-0.425
721	-0.043
721	-0.045
740	0.378
740	0.362
748	0.486
751	0.517
760	0.580
760	0.585
770	0.611
770	0.624
779	0.636
780	0.610
790	0.585
800	0.535
800	0.539
800	0.578
801	0.591
820	0.399
820	0.374
850	0.077
850	0.088
875	-0.084
875	-0.093
899	-0.243
900	-0.231

Table 13 Regressing Lead-Lag Mode Damping, Case 3

Ω, rpm	$\sigma_{\zeta r_1}$ sec^{-1}
529	-1.10
549	-1.57
552	-1.40
591	-0.659
600	-0.710
601	-0.597
601	-0.636
610	-0.835
650	-1.25
650	-1.46
651	-1.32
673	-1.60
700	-0.819
700	-0.898
721	-0.043
721	0.005
741	0.388
750	0.462
760	0.559
770	0.542
772	0.499
781	0.480
799	0.338
809	0.205
810	0.183
830	-0.243
850	-1.12
850	-1.28
899	-1.96
900	-2.13

Table 14 Explanation of Prediction Codes

ID	Prediction Method	User
BH	DRAV21	Bell Helicopter Textron
BV	C-90	Boeing Vertol
HH_1	DART	Hughes Helicopters
HH_2	E927-1	Hughes Helicopters
SA_1	G400	Sikorsky Aircraft
SA_2	E927-2	Sikorsky Aircraft
SA_3	E927-3	Sikorsky Aircraft
AL	FLAIR	U.S. Army Aeromechanics Laboratory
NA	CAMRAD	NASA Ames Research Center

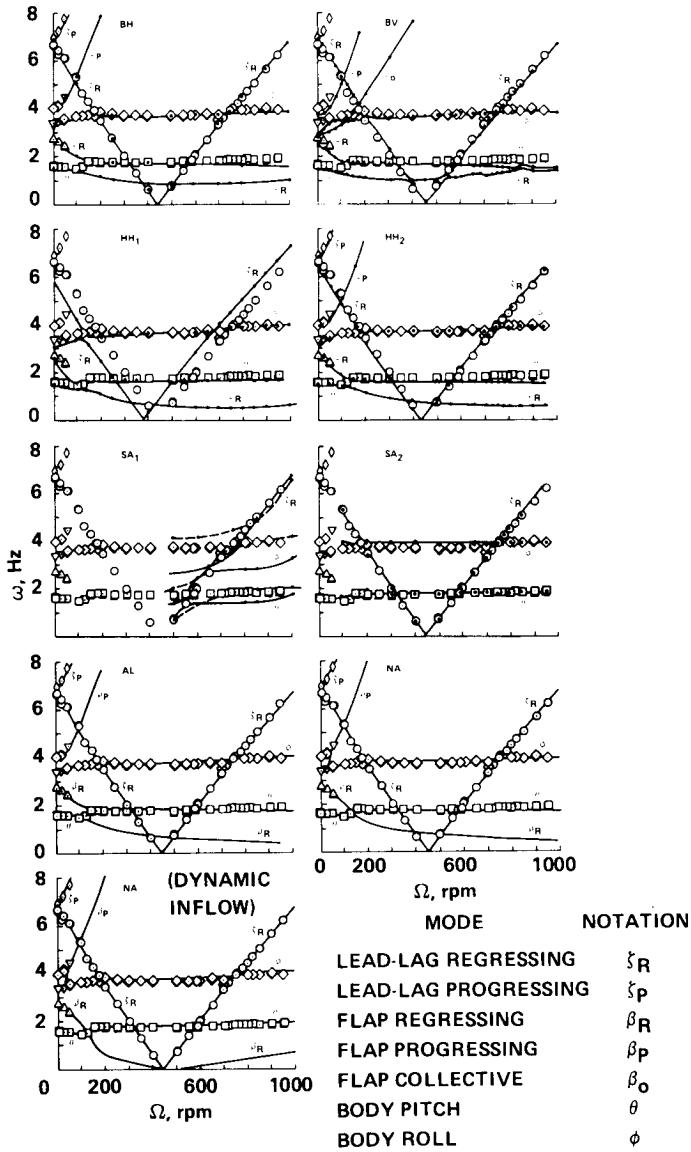

Fig. 11 Individual comparison for Case 1 modal frequencies.

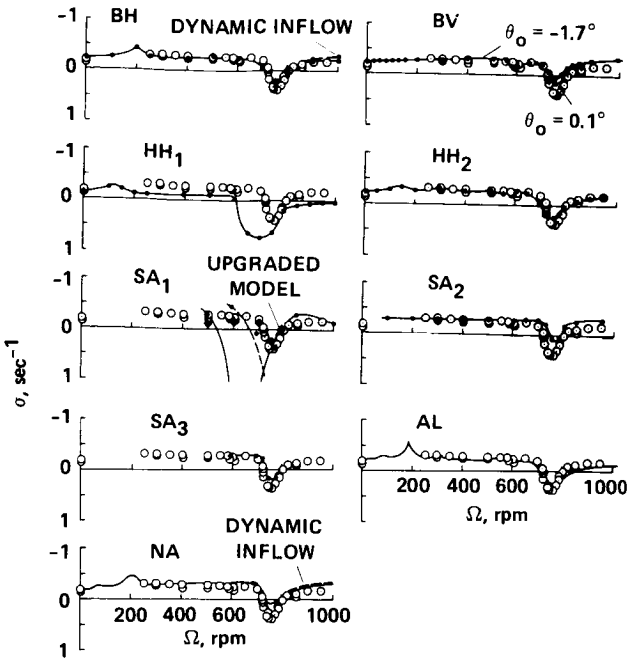

Fig. 12 Individual comparison for Case 1 regressing lead-lag damping.

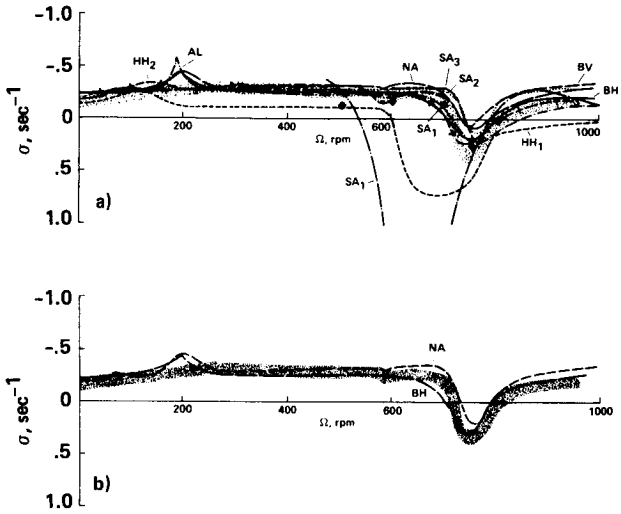

Fig. 13 Composite comparison for Case 1 regressing lead-lag damping. a) Without dynamic inflow. b) With dynamic inflow.

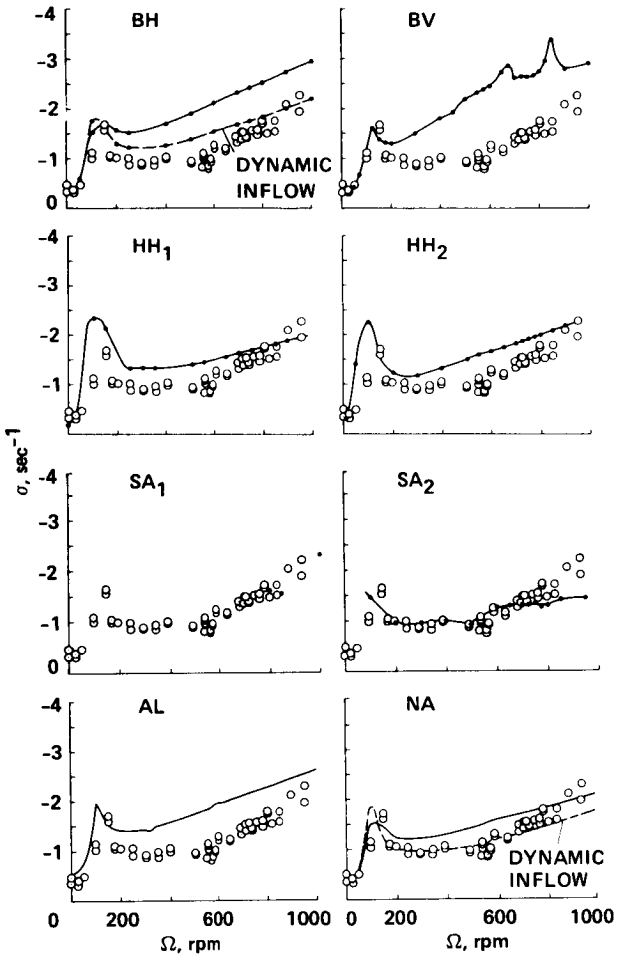

Fig. 14 Individual comparison for Case 1 body pitch-mode damping.

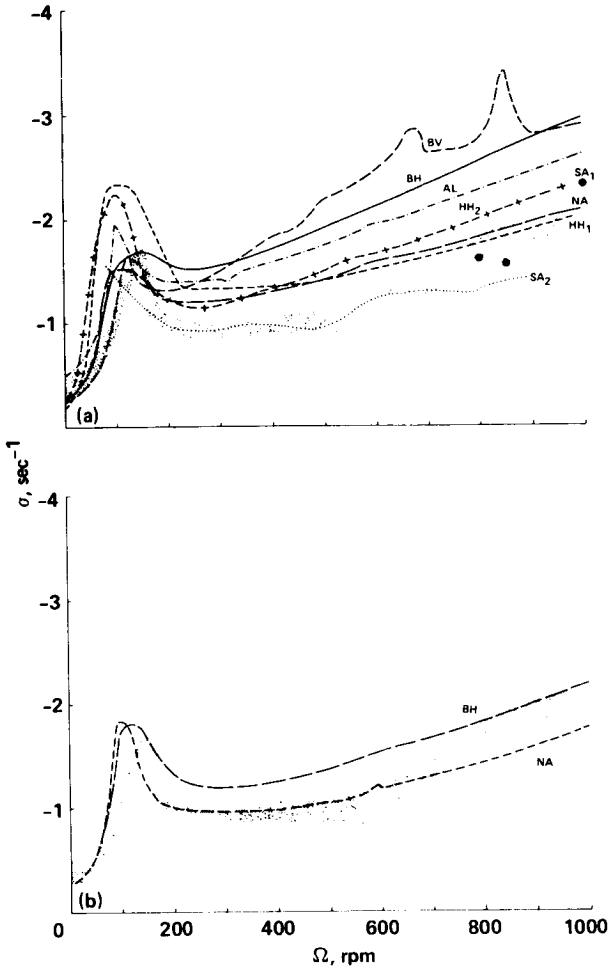

Fig. 15 Composite comparison for Case 1 body pitch-mode damping. a) Without dynamic inflow. b) With dynamic inflow.

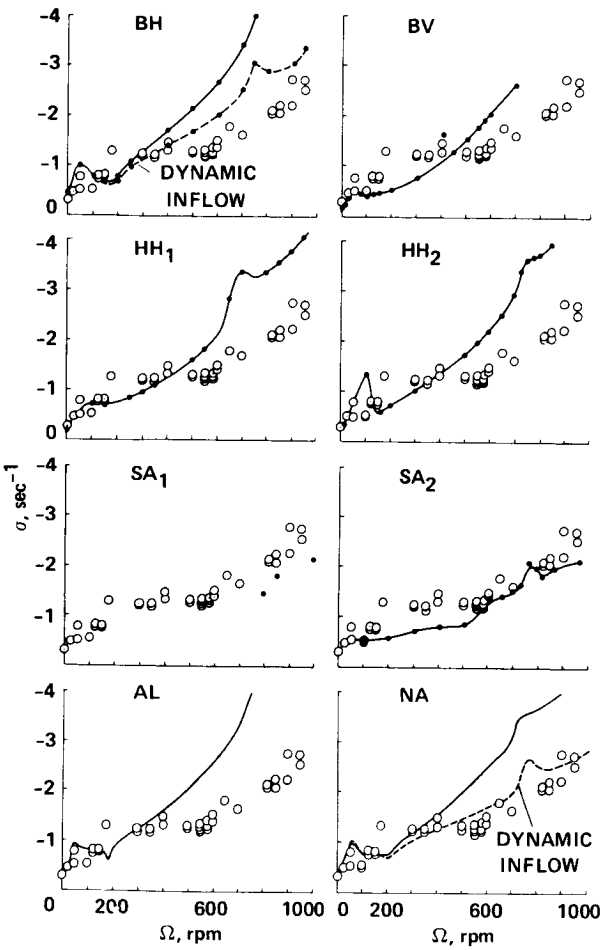

Fig. 16 Individual comparison for Case 1 body roll-mode damping.

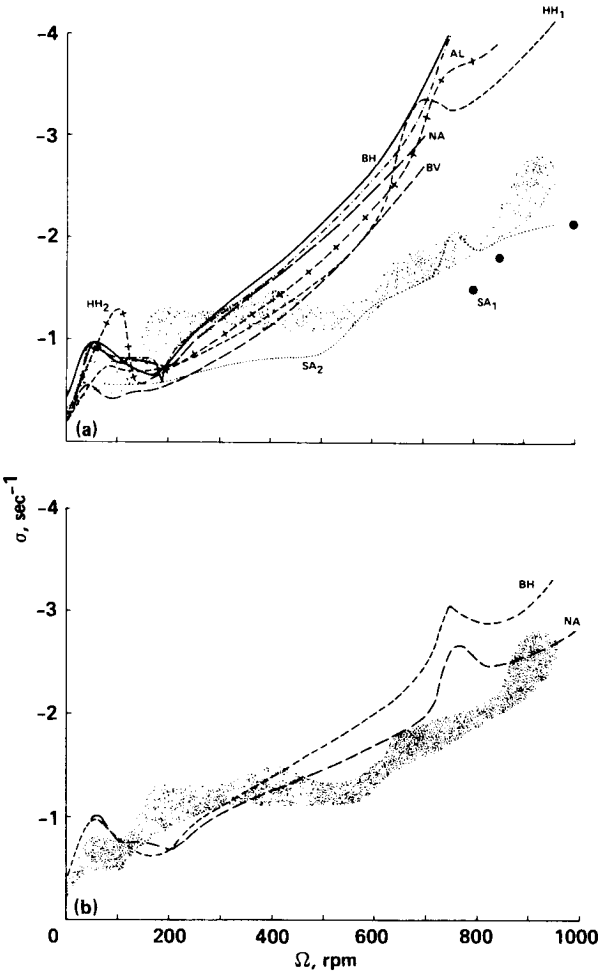

Fig. 17 Composite comparison for Case 1 body roll-mode damping. a) Without dynamic inflow. b) With dynamic inflow.

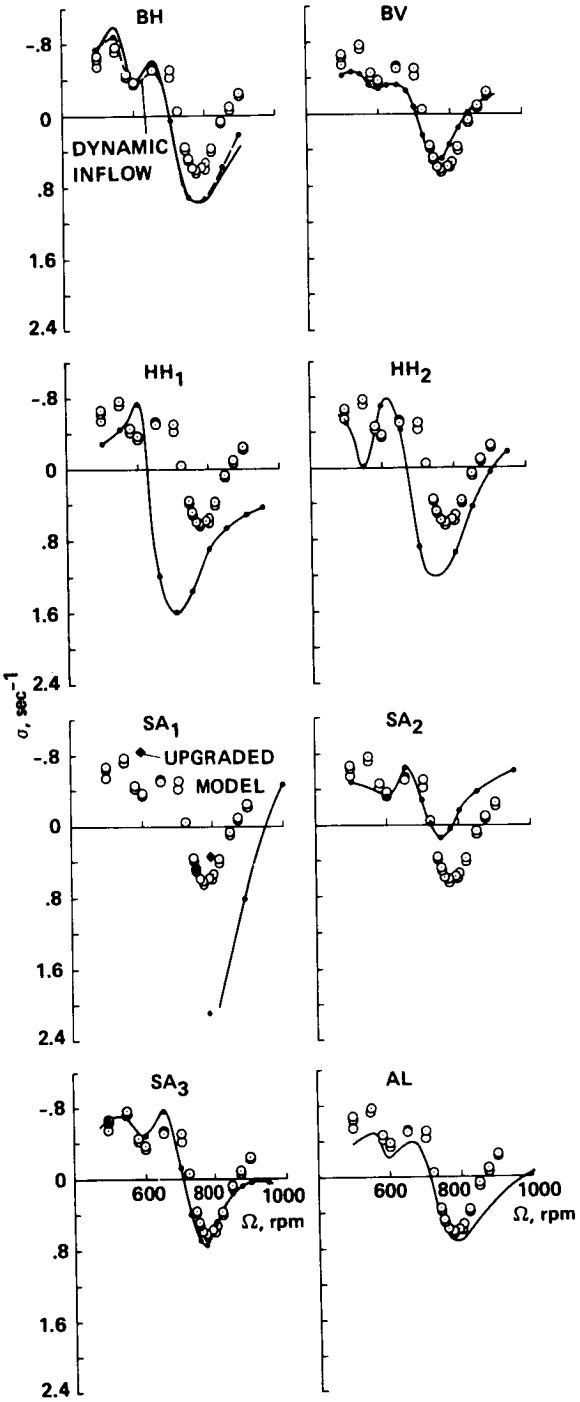

Fig. 18 Individual comparison for Case 2 regressing lead-lag damping.

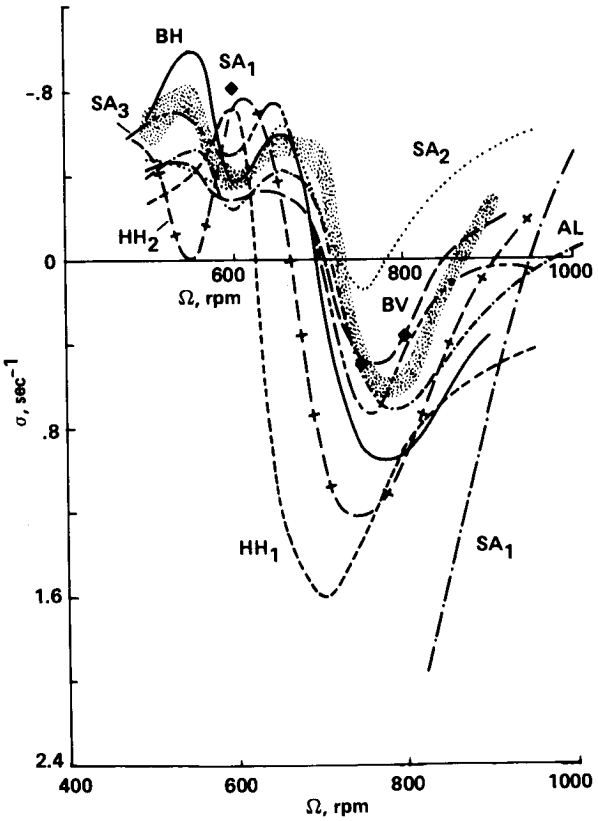

Fig. 19 Composite comparison for Case 2 regressing lead-lag damping.

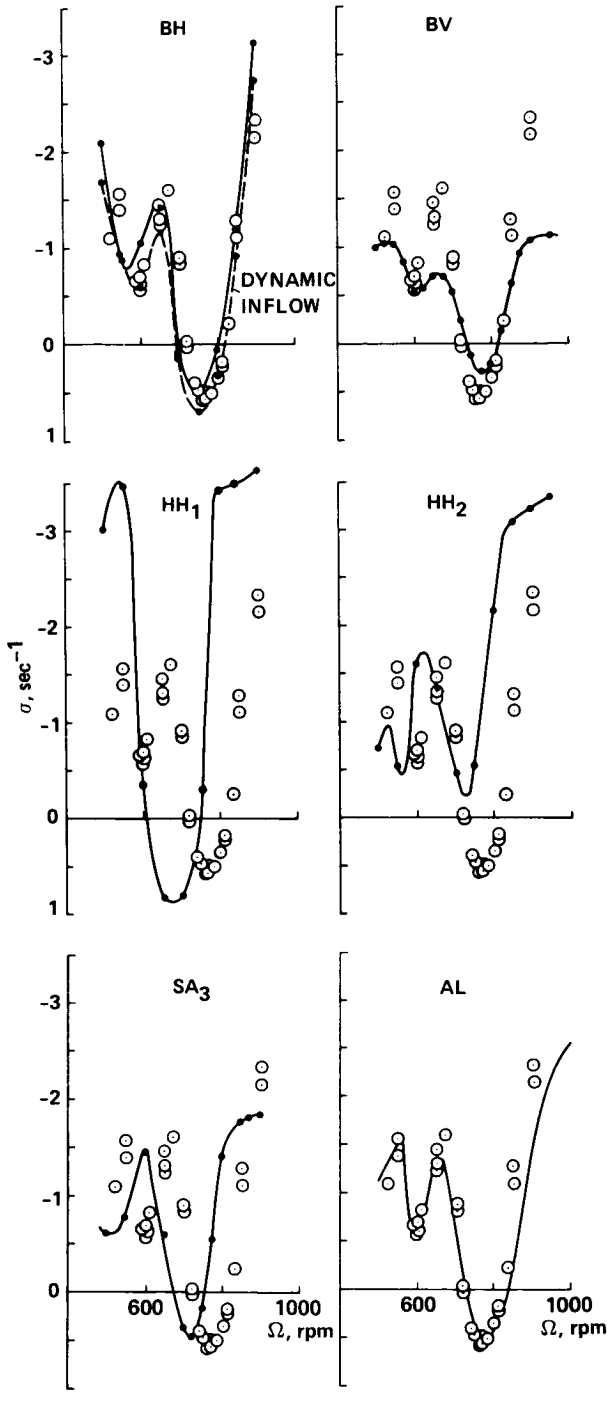

Fig. 20 Individual comparison for Case 3 regressing lead-lag damping.

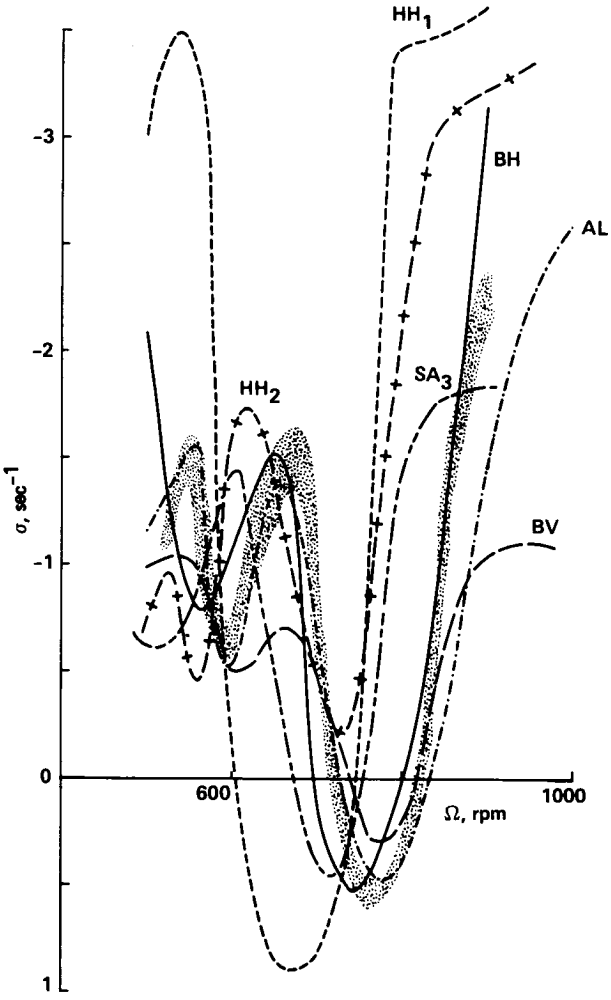

Fig. 21 Composite comparison for Case 3 regressing lead-lag damping.